Proceedings of the ASME 2012 International Manufacturing Science and Engineering Conference
MSEC2012
June 4-8, 2012, Notre Dame, Indiana, USA

MSEC2012-7307

DETECTION OF CUTTING PHENOMENA USING SENSOR FUSION

J. A. Slotwinski[1], G. W. Vogl, and R. W. Ivester
National Institute of Standards and Technology (NIST)
Engineering Laboratory
Gaithersburg, MD, USA
[1]Contact Author

I. M. Younker
Lebanon Valley College
Annville, PA, USA

KEYWORDS

Sensor Fusion, Cutting Phenomena, Chip Segmentation, Accelerometer, Acoustic Emission Sensor, Ultrasonic Sensor, Strain Gage

ABSTRACT

This paper presents an investigation of the application of a suite of sensors for simultaneous *in-situ* measurements of machining processes. While not every individual sensor responds to all machining phenomena, the suite of sensors together responds to many machining phenomena of interest, including chip segmentation, chip breakage, and vibrations. The simultaneous use of a suite of sensors with modest data-acquisition equipment and the use of careful preliminary laboratory testing for optimizing sensor performance distinguishes this present proof-of-concept work from prior process monitoring efforts using individual sensors. This paper includes a discussion of pre-deployment laboratory measurements and a full description of the instrumented tool holder, associated circuitry, and data analysis methods. The deployment of multiple sensors of varying sophistication and cost lays a technical foundation for the ultimate objective of industrially practical measurement and monitoring systems for metal cutting processes.

INTRODUCTION

The capability to produce parts faster with higher quality and less expense requires technical advances in several areas, including process monitoring, closed-loop feedback control, tool condition monitoring, and real-time monitoring of the health of production systems. Sensors provide the common thread for all of these capabilities. Modern-day sensors possess attractive characteristics for these applications, including improved robustness and decreased cost and size. These capabilities facilitate ease of insertion into manufacturing equipment and tools. Coupled with affordable and rapid digital equipment for acquiring and storing large data sets, as well as fast computers for data analysis and modeling, the appeal of sensors in industrial applications is clear. However, the correlation of sensor data with process phenomena or equipment state presents a major challenge.

There is a considerable body of work on monitoring of manufacturing processes, including Teti's recent comprehensive review [1], and multiple examples of using sensor fusion [2-4], but most of the efforts have focused on single sensors.

This work has an ultimate objective of developing industrially practical measurement systems using a suite of sensors simultaneously with modest data acquisition (DAQ) equipment. This paper focuses on developing the technical basis for detecting chatter, chip segmentation, and chip breakage during metal turning, with possible future work to address tool wear and the correlation of sensor signals with part surface quality. Future work could also include developing these sensors into one or more embedded, small, and wireless sensor system packages.

OVERVIEW OF SENSORS

Figure 1 shows all six sensors in their final placements for the sensor fusion proof of concept (POC). For each machining test, eight sensors acquired signals: an acoustic emission (AE) sensor, a thin-film polyvinylidene fluoride (PVDF) ultrasonic sensor, a semiconductor strain gage, a piezoelectric strain sensor, a thermocouple, and a triaxial (three signals) accelerometer.

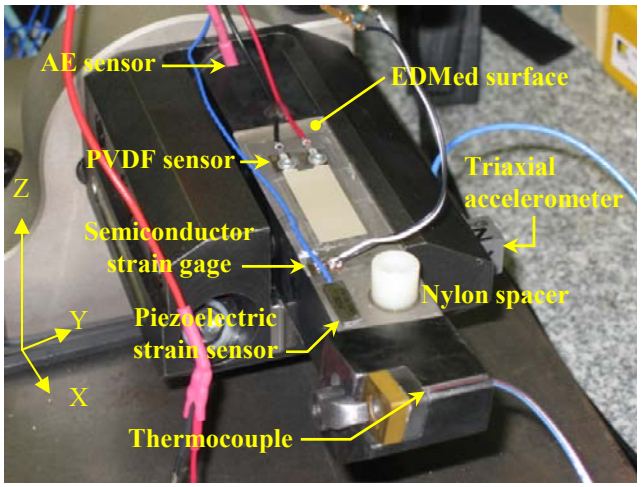

FIGURE 1 – INSTRUMENTED INSERT HOLDER (SHANK)

Three circuits on a custom printed circuit (PC) board provided on-board power and processing for the semiconductor strain gage, AE sensor, and PVDF sensor. Figure 2 shows the elevation of the PC board above the sensors to provide clearance for protecting wire connectors. As seen in Figure 3, the circuit board extends beyond the envelope of the insert holder and tool holder. For the experiments in this paper, the path of the tool relative to the workpiece and collet holder avoided interference with the circuit board. Connecting the sensors to their circuits with pin connectors and circuit outputs to the DAQ devices via Bayonet Neill–Concelman (BNC) connectors enabled easy removal of the circuit board from the sensors and DAQ equipment.

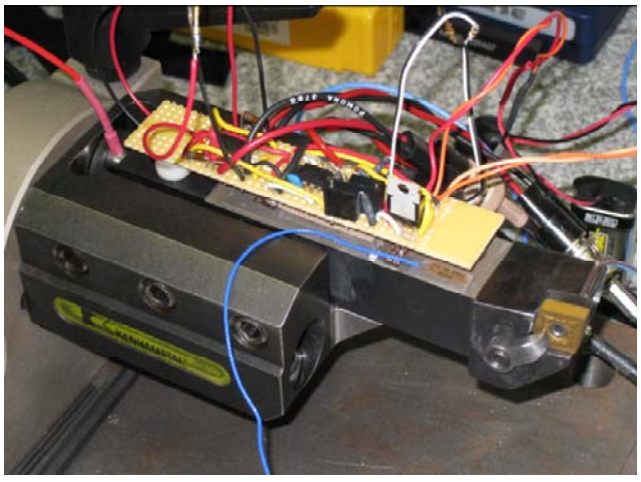

FIGURE 2 – PRINTED CIRCUIT BOARD ON INSERT HOLDER

The suite of sensors together provides sensitivity to many machining phenomena of interest due to overlapping bandwidths. Figure 4 shows representative bandwidths for the sensors, obtained primarily from manufacturers' specifications. (Some supplemental laboratory measurements were also made.)

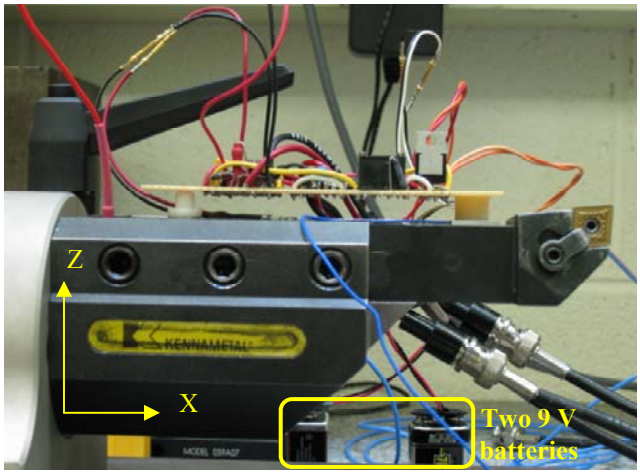

FIGURE 3 – SIDE VIEW OF SENSORS ON TOOL

As seen in Figure 4, at least one sensor can detect signals in any frequency within the bandwidth from 0 Hz to 100 kHz. No sensor spans the entire bandwidth, but together the sensor system spans the desired frequency range. The fused sensors should thus be sensitive to machining phenomena of interest, including chatter in the 1 kHz to 20 kHz range, segmentation in the cut chips with a frequency of roughly 15 kHz, and chip breakage frequencies around 400 Hz.

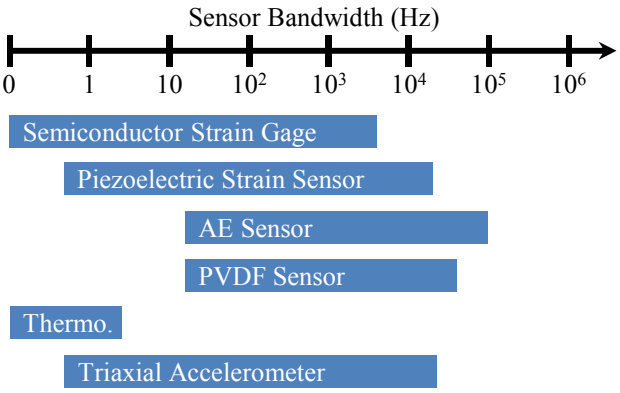

FIGURE 4 – COMPARISON OF SENSOR BANDWIDTHS

DESCRIPTION OF SENSORS

PIEZOELECTRIC STRAIN SENSOR

A commercially available integrated electronic piezoelectric (IEPE) strain sensor (attached with cyanoacrylate adhesive parallel to the X-axis) has a nominal sensitivity of 50 mV/με as calibrated by the manufacturer with a strain gage reference method. The sensor has a frequency response range from 0.5 Hz to 100 kHz and an output voltage range of ±5 V, equivalent to about ±100 με.

TRIAXIAL ACCELEROMETER

An IEPE triaxial accelerometer (PCB Piezotronics Inc., model YJ356A22) attached with cyanoacrylate (Loctite® 454™) has nominal sensitivities in all three axial directions of 100 mV/g (10.2 mV/(m/s^2)) as calibrated by the manufacturer. The three output channels have an output voltage range of ±5 V, equivalent to about ±50 g in all three axial directions. The accelerometer has a linear (±5 percent) frequency response range from 0.5 Hz to 4 kHz for all three calibrated directions. The resonant frequency specified as being at least 25 kHz provides adequate bandwidth to capture the full range of segmentation frequencies up to about 20 kHz.

THERMOCOUPLE

Modification of the insert holder (tool shank) and the insert shim enabled positioning a type T (copper-constantan) thermocouple close to the cutting edge while protecting it from the cutting process. Placing the thermocouple in the shim rather than the cutting insert reduces sensitivity to the process but improves practicality by enabling changing the insert with minimal effort. As shown in Figure 5, a 2 mm width channel near the front edge of the tool shank head with an accompanying 2 mm diameter hole in the shim locates the thermocouple joint on the order of a millimeter from the nose of the insert.

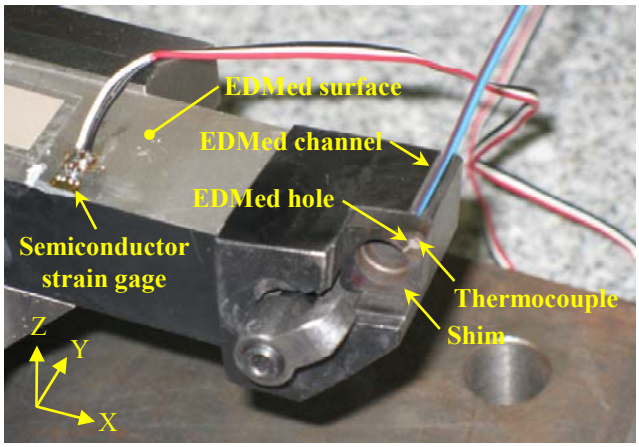

FIGURE 5 – THERMOCOUPLE AND SEMICONDUCTOR STRAIN GAGE SENSOR

In order to improve the thermocouple response to process changes, liberal application of solder (thermal conductivity (k) = 50 W/m·K [5]) in the shim hole and heat sink compound (k = 0.58 W/m·K) under the insert minimizes thermal barriers due to air (k = 0.025 W/m·K [6]). The type T thermocouple measures temperatures from -200 °C to 350 °C with a nominal sensitivity of 40 µV/K at 20 °C [6].

SEMICONDUCTOR STRAIN GAGE

A semiconductor strain gage (BCM Sensor Technologies b.v.b.a., model SB4-350-3.8-P-2) attached with cyanoacrylate parallel to the X-axis (Figure 5) has a nominal resistance of 350 Ω and a nominal gage factor (GF) of 130. The manufacturer specifies the maximum working current and strain limit as 10 mA and 6000 µε, respectively. Among the sensors in this work, only the semiconductor strain gage detects force-related signals down to 0 Hz and thus is the only sensor in this work that can detect average cutting forces.

AE SENSOR

Despite their original application for non-destructive evaluation (NDE) of materials and structures in relatively quiet environments, AE has been applied successfully for manufacturing process monitoring [7, 8]. The rapid release of elastic strain energy in the cutting tool during chip breakage and shear localization in turning operations produces a source of potentially detectable acoustic energy [9].

As seen in Figure 6, a Physical Acoustics Micro-80S acoustic emission sensor attached to the back of the shank with water-soluble acoustic couplant detects signals from about 10 Hz to 100 kHz. Proper functioning of the AE sensor requires electrical isolation from the mounting surface (see specifications for Micro80S sensor in Ref. [10]) as well as the back of the shank holder by a rubber disk (see Figure 6).

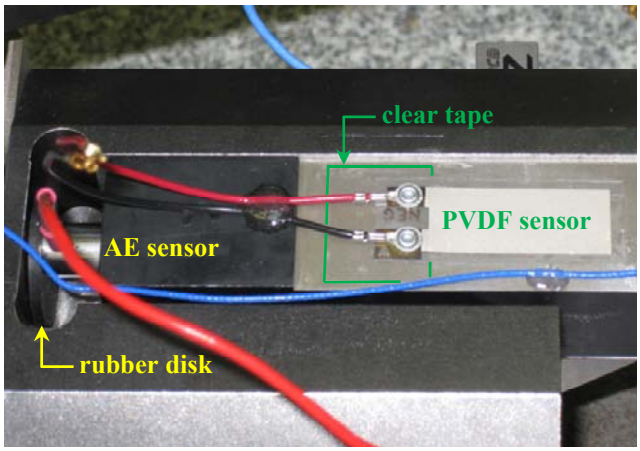

FIGURE 6 – AE AND PVDF SENSORS

PVDF SENSOR

Thin-film polymer ultrasonic transducers provide many appealing characteristics for process monitoring applications, including physical flexibility and very low cost, allowing for versatile insertion into various manufacturing systems. PVDF sensors have shown promise for detecting chip segmentation in metal cutting [11].

Attachment of a standard DT1 element size PVDF sensor (12 mm x 30 mm active area) with non-conductive double-sided tape to the tool shank (Figure 6) provided electrical isolation, as required for proper functionality. A small amount of epoxy provided strain relief and a piece of clear tape provided electrical isolation for the two sensor leads.

DESCRIPTION OF SENSOR CIRCUITS

SEMICONDUCTOR STRAIN GAGE CIRCUIT

The 350 Ω semiconductor strain gage was placed as one leg of a quarter-bridge (Wheatstone bridge) configuration shown in Figure 7.

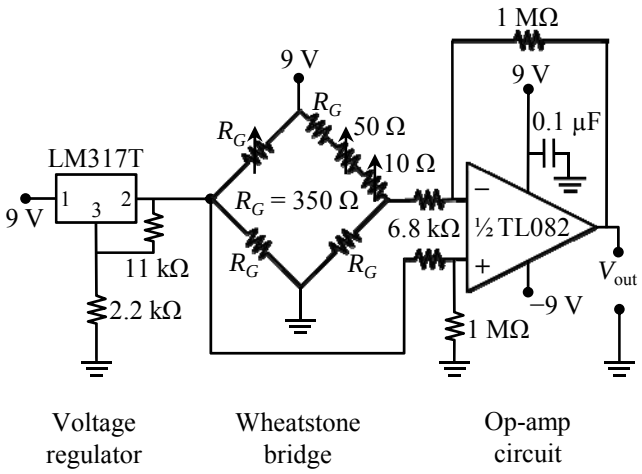

FIGURE 7 – SCHEMATIC OF CIRCUIT FOR SEMICONDUCTOR STRAIN GAGE

The semiconductor strain gage bridge excitation voltage must be sufficiently low to minimize voltage drift and changes in gage factor due to temperature, yet high enough to maximize signal-to-noise from the bridge output. A bridge excitation of 1.5 V was found to provide adequate signal while minimizing drift and temperature change. An adjustable voltage regulator (National Semiconductor, model LM317T) with two resistors (2.2 kΩ and 11 kΩ) lowered the bridge excitation voltage from 9 V to 1.5 V, leading to approximately 2 mA of current through the semiconductor strain gage.

Two variable potentiometers, one 50 Ω and another 10 Ω, placed in series in the leg "mirrored" to the semiconductor leg in the Wheatstone bridge enabled gross and fine adjustments to balance the bridge circuit.

The bridge output is amplified via a high speed junction field-effect transistor (JFET) input operational amplifier. The operational amplifier is actually a dual operational amplifier, so only one half (1/2) of the op amp is used for the semiconductor strain gage circuit. The gain was set by choosing values for the two pairs of resistors in the op amp such that a constant force of about 5000 N in the negative Z-direction induces an output voltage (V_{out}) of 5 V. The approximate sensitivity of the strain gage circuit is 1 mV/N, and the peak-to-peak noise of about 10 mV at a sampling rate of 51.2 kHz correlates to a force measurement noise of about ±5 N.

AE AND PVDF CIRCUITS

The piezo-based AE and PVDF sensors have very high capacitive impedances for our sub-MHz frequency range of interest. These high impedances prevent proper measurement via direct DAQ connection because the impedance of the device being measured should be much lower than that for the voltmeter. Consequently, the sensor signals must pass through a voltage follower or similar op amp circuit to transform the high-impedance voltages to low-impedance voltages, thus enabling a voltmeter to measure the signals without influencing them significantly.

Over the ±9 V range of the DAQ system, the AE and PVDF sensor sensitivities tuned to approximately 2 mV/N through non-inverting voltage amplifier circuits [12] (Figure 8) with amplifier gain tuning via feedback resistor selection avoided saturation for impulses up to ±4500 N. High-pass filtration at roughly 10 Hz allowed detection of signals at chip breakage frequencies estimated at 400 Hz.

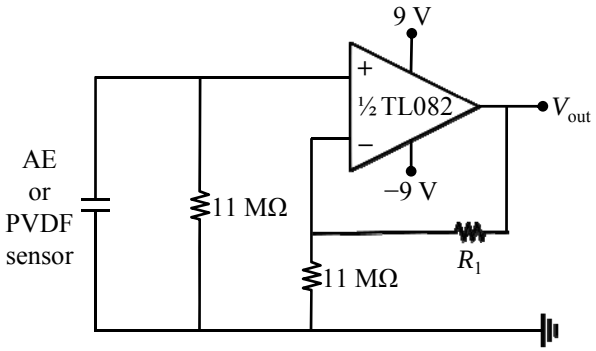

AE sensor: R_1 = 100 MΩ
PVDF sensor: R_1 = 11 MΩ

FIGURE 8 – SCHEMATIC OF AE AND PVDF SENSOR CIRCUITS

LABORATORY TESTING OF SENSORS

The typical machining environment generates many mechanical and electrical signals detectable by the sensors used in this work. These signals include phenomena of interest (such as chip segmentation, chip breakage, etc.) as well as confounding signals (such as electromagnetic signatures from a machine's internal systems.) While acquiring signals with the sensors is relatively easy, correlating those signals with the machining phenomena of interest in the presence of much larger magnitude confounding signals presents a major challenge. Careful sensor characterization and testing of the sensor suite with synthetic, well-understood inputs similar to those encountered in the actual in-machine environment provide a sound technical basis for the essential task of discriminating confounding signals from signals of interest. This preliminary laboratory testing also ensures that the data acquisition hardware and software function as expected in an environment free of spurious signals. This section includes coherence testing for optimizing sensor placement, but excludes additional sensor characterization using synthetic signals for brevity.

A calibrated impact hammer (Kistler Instrument Corporation, model 9722A500) generated measured force impulses on the cutting tool insert for subsequent coherence and sensitivity analyses of the sensors. Multiple trials with each sensor in various positions provided a systematic statistical basis for optimal sensor placement.

PERFORMANCE METRICS

The sensitivities and coherences of the sensor outputs with respect to the measured force signals provided performance metrics for evaluating sensor positions. For any trial, processing the fast Fourier transforms (FFTs) of impact force and sensor output signal ($F(\omega)$ and $A(\omega)$ respectively) yielded single-sided frequency spectra [13]:

$$G_{xx}(\omega) = F^*(\omega)F(\omega) \quad (1)$$
$$G_{xy}(\omega) = F^*(\omega)A(\omega) \quad (2)$$
$$G_{yx}(\omega) = A^*(\omega)F(\omega) \quad (3)$$
$$G_{yy}(\omega) = A^*(\omega)A(\omega) \quad (4)$$

where a superscript asterisk (*) denotes the conjugate of the complex number. For each set of impact data, ratios of the average spectra yield two different measures of the frequency response function (FRF) called H_1 and H_2:

$$H_1(\omega) = \frac{\bar{G}_{xy}}{\bar{G}_{xx}} \quad (5)$$
$$H_2(\omega) = \frac{\bar{G}_{yy}}{\bar{G}_{yx}} \quad (6)$$

where an overbar denotes the arithmetic average function. Larger magnitudes of $H_1(\omega)$ represent higher sensitivity, or signal-to-noise ratios. The coherence function, $\gamma^2(\omega)$, calculated as the ratio between $H_1(\omega)$ and $H_2(\omega)$:

$$\gamma^2(\omega) = \frac{H_1(\omega)}{H_2(\omega)} \quad (7)$$

provides a quantitative measure of how well the output relates to the input.

Coherence values very close to 1 (e.g., $\gamma^2 > 0.995$) indicate strong coherence of the sensor response to the force. Relative evaluation of each sensor at various positions involves assessing changes in sensitivity through $H_1(\omega)$ and coherence through $\gamma^2(\omega)$.

TRIAXIAL ACCELEROMETER

Figure 9 shows four tested accelerometer positions in addition to the final position (see Figure 1). Wax affixed the accelerometer to the tool shank for ease of relocation. For each of the five positions, two different impulses (one incident to the tool holder and one at roughly 45°) measured three times each provided statistically meaningful data.

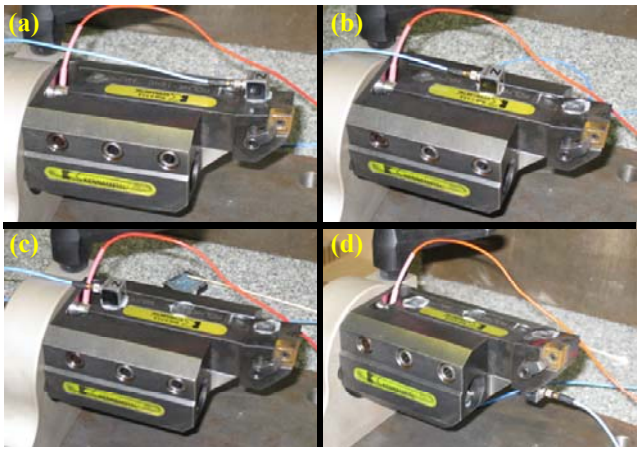

FIGURE 9 – TESTING OF ACCELEROMETER AT VARIOUS POSITIONS ON SHANK

Figure 10 shows the coherence magnitude of the Z-axis triaxial accelerometer signal with respect to a perpendicular impact force on the cutting insert with the accelerometer in the position shown in Figure 1, as employed during the subsequent cutting tests. The coherence of the acceleration signal remains fairly close to 1 until reaching a roll-off frequency. The coherence results for the other two axes were similar. This location had better coherences than the other positions as well as one of the greatest sensitivities.

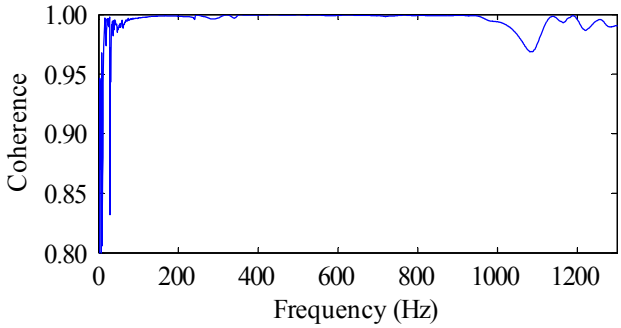

FIGURE 10 – COHERENCE MAGNITUDE OF Z-AXIS ACCELEROMETER OUTPUT WITH RESPECT TO TRIAL FORCE INPUT

AE SENSOR

Similar testing of the AE sensor determined that stress waves propagate effectively through the tool. All tested positions on the tool provided equivalent AE sensor performance metrics, so placing the AE sensor on the back of the tool shank maximized convenience. Pre-loading the AE sensor between the shank on one side and a rubber disk against the tool holder body on the opposite side robustly held the sensor in place.

THERMOCOUPLE

Placement of the thermocouple required close proximity to the cutting edge to maximize sensitivity while providing

protection from chips and maintaining structural integrity of the shim during machining. The channel and hole satisfied these criteria effectively. Both the thermocouple and the shim remained undamaged during subsequent machining. Laboratory testing prior to cutting determined the time constant of the thermocouple to be 0.13 s ± 0.02 s.

PVDF SENSOR

The relatively large size of the PVDF sensor required the full width of the tool shank surface and a substantial portion of its length. Laboratory testing revealed no significant advantage in sensor performance for any position, so placement of the PVDF sensor at the back end of the shank provided space near the front end for the two strain sensors.

STRAIN SENSORS

Finally, as seen in Figure 1, placement of the two strain sensors maximized sensitivity and coherence for both. Mutual alignment provided very similar strains and served as a valuable check during data analysis.

DATA ACQUISITION HARDWARE AND SOFTWARE

Several National Instrument DAQ devices and a laptop computer running a customized LabVIEW software interface were used to acquire sensor data: PVDF and AE data at 200 kHz using a 16-bit DAQ device, strain and accelerometer data at 51.2 kHz using 24-bit DAQ devices, and thermocouple data at 7 Hz with a 24-bit device. The laptop used for data acquisition had a 2.66 GHz processor and 4.0 GB of random-access memory. Memory limitations associated with acquiring multiple channels simultaneously restricted acquisition to approximately 2 seconds for each trial. Proper design of the cutting tool path enabled acquisition of entire cutting trials, including entry, mid-cut, and exit signatures.

CUTTING TESTS

After fully instrumenting the tool with sensors and their circuits, the addition of plastic protectors provided protection from the hot, sharp chips generated during cutting. Wires and BNC connectors near the back of the tool shank remained exposed. Dry cutting avoided the need to protect the sensors and circuits from liquids. Future industrially practical implementation would require wireless sensors and robust protection from liquids.

However, the BNC cables connecting the instrumented tool to the DAQ system needed to be bundled and protected from the chips. Thus, after placement of the instrumented tool in the turning center, a flexible plastic tube was used to shield the cables to the DAQ system.

Data acquired with the Mazak Integrex® 100-IV turning center powered on and the spindle turning, but without any cutting provided a measure of the environmental noise. Cutting experiments included systematic combinations of Al 6061-T6, 1045 steel, and stainless steel materials, a depth of cut of 2 mm (0.08 in), a variety of feed rates (0.20 mm/rev [0.008 in/rev] – 0.30 mm/rev [0.012 in/rev]) and surface speeds (1.4 m/s [275 ft/min] – 4.2 m/s [825 ft/min]), and no coolant. Fifty-two distinct cutting trials led to collection of 1.4 gigabytes of sensor data. Collection of chips from each trial enabled subsequent analysis. Table 1 shows the cutting parameters for eight representative trials.

TIME RECORDS

For each trial, plotting the raw data from each sensor provided visualization of the data in preparation for further analysis. The noisy raw unprocessed data streams made identification of cutting phenomena in the data difficult. However, the raw data clearly show the tool entry, steady state cutting, and exit. For example, most of the typical data signals show the cutting entry and exit as in Figure 11. Note that the staircase like nature of the temperature data results from the sample-and-hold nature of the thermocouple's DAQ device.

TABLE 1 – CUTTING PARAMETERS FOR EIGHT TRIALS

Trial	Material	Depth of Cut (in)	Feed Rate (in/rev)	Spindle Speed (RPM)	Surface Speed (ft/min)
1	Al 6061-T6	0.08	0.08	2838	825
2	Al 6061-T6	0.08	0.08	3317	825
3	Al 6061-T6	0.08	0.08	5650	459
4	Al 6061-T6	0.08	0.08	1654	550
5	1045 Steel	0.08	0.012	5002	825
6	1045 Steel	0.08	0.012	5650	695
7	1045 Steel	0.08	0.012	5650	459
8	Stainless Steel	0.08	0.012	1667	275

The signals in Figure 11 detect many of the same cutting events despite their quantitative and qualitative differences. Specifically, the semi-conductor and piezoelectric strain gages appear very similar for frequencies greater than 0.5 Hz (see Figure 4). The semi-conductor strain gage signal in Figure 11 steadies out during cutting, while the piezoelectric strain signal damps out during cutting because it cannot maintain a DC signal.

The root mean square (RMS) outputs for the AE and PVDF sensors were calculated for 0.5 s of steady-state cutting, and the results are shown in Figure 12, which shows that correlations exist between the AE and PVDF RMS outputs and the material removal rate. As seen in Figure 12, the RMS outputs increase somewhat linearly with the material removal rate. Even though the AE sensor correlates slightly better than the PVDF sensor for the three materials tested, the inexpensive PVDF sensor basically captures the same trend as the more expensive AE sensor.

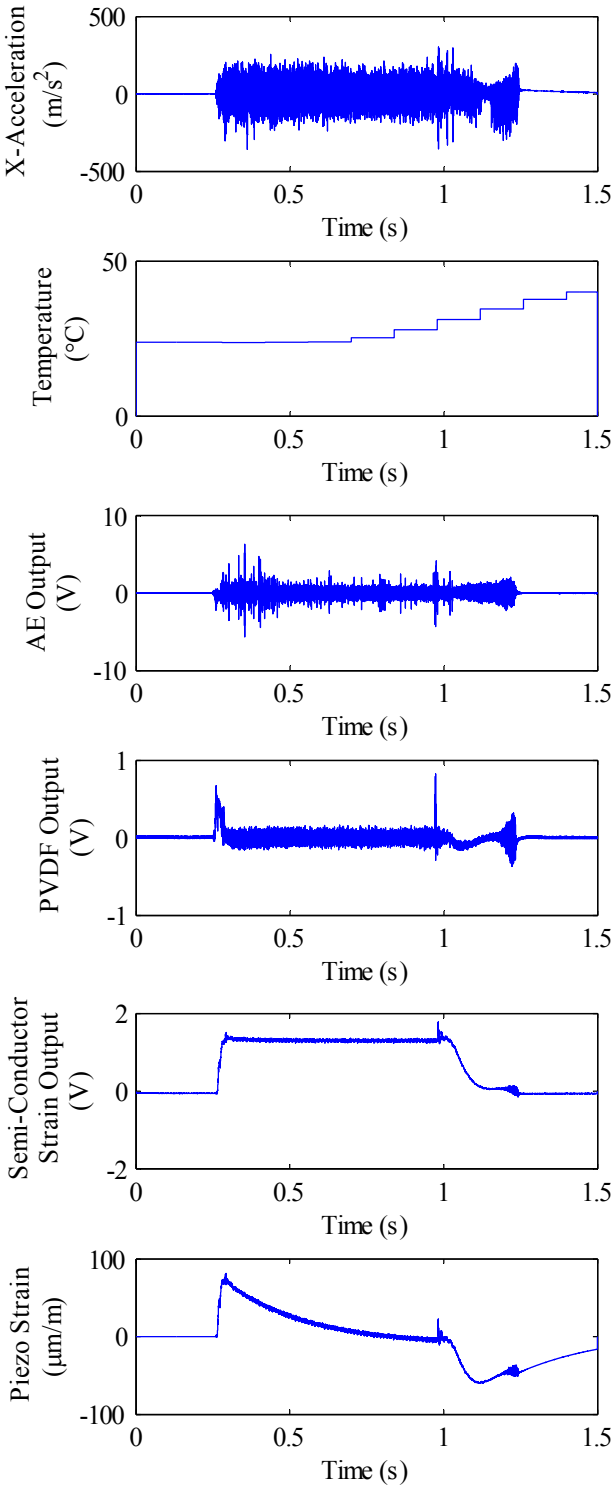

FIGURE 11 – TYPICAL DATA FOR SIX OF THE EIGHT SENSOR SIGNALS (Y- AND Z-ACCELERATIONS NOT SHOWN)

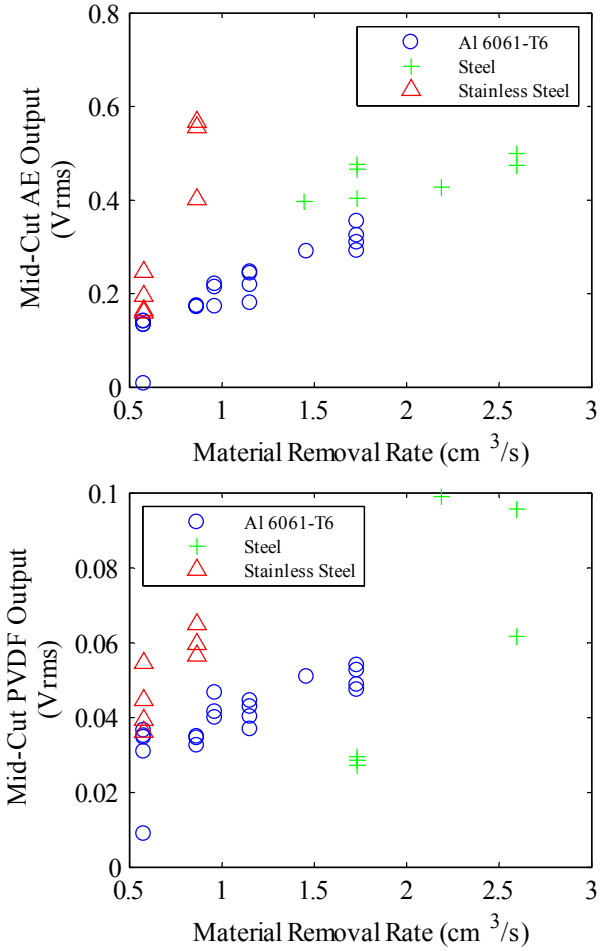

FIGURE 12 – AE AND PVDF OUTPUTS VERSUS MATERIAL REMOVAL RATE

SPECTRAL ANALYSIS AND SMOOTHING

The spectral content of each time record, obtained by applying a FFT to the raw time records, revealed many prominent peaks in the noisy spectra. The application of several spectral smoothing techniques [14] enhanced confidence in peak identification. Figure 13 shows the FFT-computed frequency content of the time record of the accelerometer's Z-axis response for one cutting trial and the results of three different smoothing techniques applied to that spectra.

The first 'combined bins' method partitions the frequency record into a number of groups given by the total number of frequency bins divided by a user-selected odd number ('compression.') Summing the amplitudes of each frequency bin lumps all of the energy within a respective group of frequencies together into the center frequency bin. The new frequency record contains only these center frequencies, discarding the others from the record. Using this computationally simple method amplifies the amplitudes of the peaks in the spectrum, allowing for easier identification.

However, this method does not preserve frequency moments[1], and may slightly shift the locations of the frequency peaks. In this case, the much smaller compression value of 35 compared to the number of data points (150 000) in the initial frequency record maintains an acceptably small shift in peak frequencies.

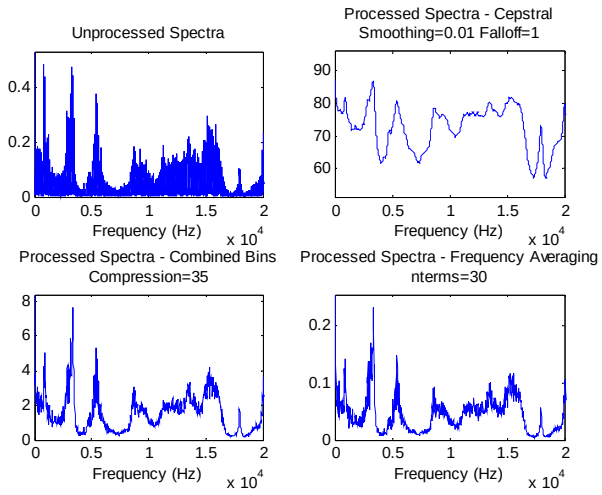

FIGURE 13 – COMPARISON OF Z-AXIS ACCELERATION UNPROCESSED SPECTRA AND THREE SMOOTHING METHODS

The second Cepstral method has its origins in speech processing. In this method the Fourier transform of the unprocessed spectra followed by an inverse Fourier transform using a windowing retains only the lower "frequencies." In essence, this method treats the original spectra like a time signal. Computing its Fourier transform and windowing in the inverse Fourier transform eliminates the noisy higher-frequency components. For the two computational parameters, Smoothing and Falloff between 0 and 1 produced the best results with a Smoothing of 0.01 and a Falloff of 1.

The final method, a moving average across the frequency bins, uses a number of frequencies equal to *nterms* in each average. This computationally simple method preserves the area under the spectral line (zeroth moment) and the mean position of the peaks (first moment), but not the second moment (line width) [14].

All three methods enhanced the identification of peaks in the spectra and seemed to be sufficient for this purpose. Additional methods such as Savitzky-Golay filtering, which has its origins in rendering visible the relative widths and heights of spectral lines in noisy spectrometric data while preserving the higher moments, could be employed for particularly noisy spectra [14]. Autoregressive modeling techniques could also be used.

Figure 14 shows a representative trial of the resulting smoothed spectra using the third (moving average) smoothing method. These data correspond to cutting 6061-T6 aluminum with a 2 mm depth of cut, a feed per revolution of 200 µm, and a spindle speed of 2838 RPM, or a frequency of 47 Hz.

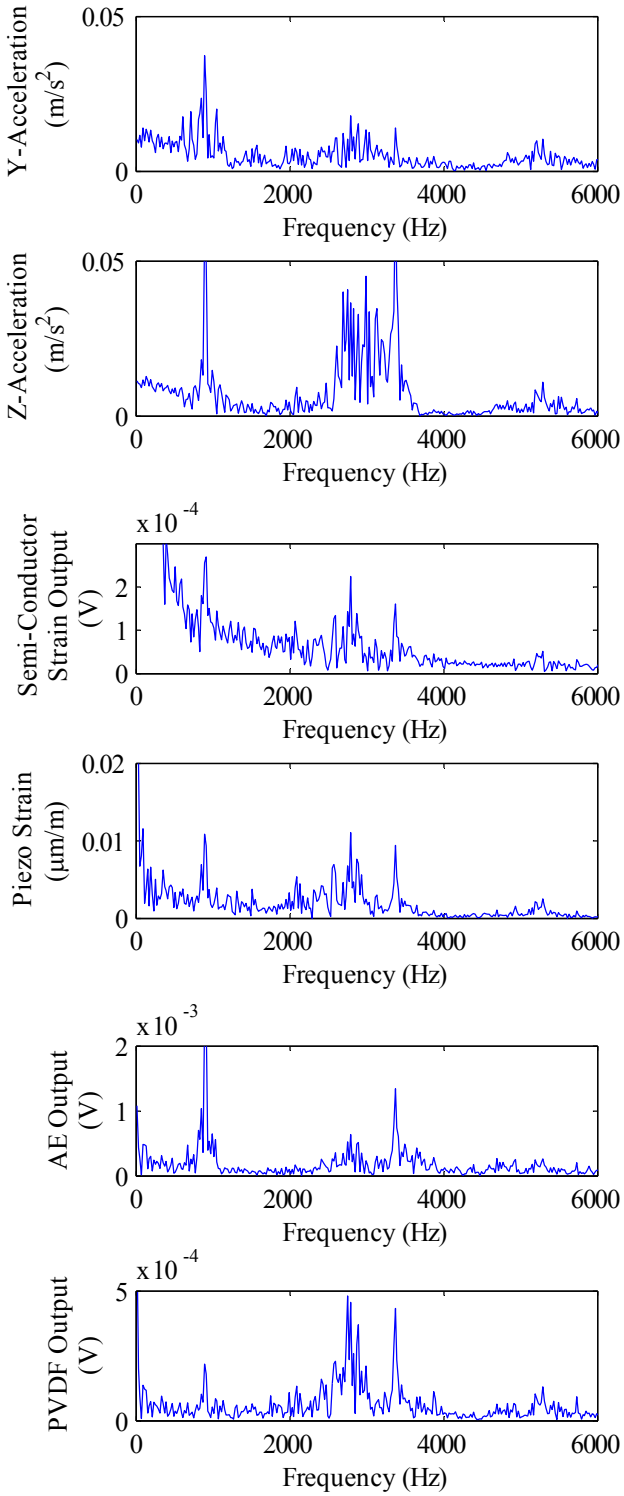

FIGURE 14 – SMOOTHED SPECTRA OF TYPICAL TRIAL DATA

[1] Zeroth moment = area under the spectral line; first moment is position along the frequency-axis; second moment is the spectral line-width.

The measured segmentation frequency (see "CHIP ANALYSIS" below) for this test of 5073 Hz falls just above the maximum estimated value of 5000 Hz. The resulting spectra showed several dominant peaks in the sensors' sensitivity ranges, and that several of the sensors measured many of the same peaks, including the segmentation frequency peaks, as well as natural resonances (at roughly 2500 Hz and 3500 Hz) of the tool holder as identified during the laboratory impact testing. Zooming in on the frequency axis of the unsmoothed spectra clearly shows the spindle frequency (f_s = 47 Hz) as well as its higher harmonic ($2f_s$).

TEMPERATURE

Thermocouple sampling at 7 Hz yielded a sampling period of about 0.14 s. A combined thermocouple time lag of 0.39 s ± 0.04 s exists due to combined effects of the thermocouple time constant, sampling period, and especially the heat transfer through the insert to the thermocouple. Subtraction of the time for the first major increase in acceleration from the time for the first detected increase in temperature determined the combined time lag. Despite a long time constant, the thermocouple captured temperature increases of 20 °C within 1 s of cutting.

Figure 15 shows the thermocouple response after 1 second of cutting for the eight trials of Table 1. For the aluminum and steel tests, the temperature increases fairly linearly with the surface speed. The nearly identical two data points for the aluminum tests with a surface speed of about 4.2 m/s demonstrate repeatability.

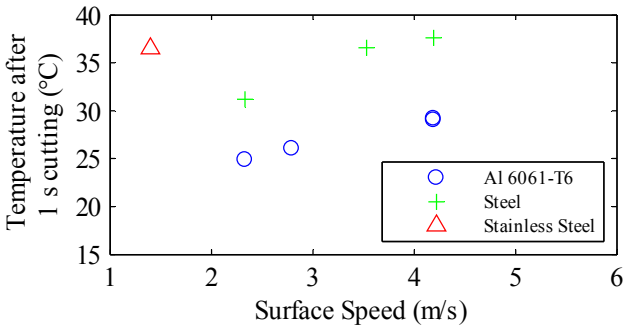

FIGURE 15 – THERMOCOUPLE TEMPERATURE AFTER 1 SECOND OF CUTTING FOR VARIOUS TRIALS

CHIP ANALYSIS

Chip analysis performed on eight of the 52 trials provided insight into sensor frequencies relevant to chip segmentation and breakage. These trials similarly show tool entry into the part. For each of these eight trials microscopic examination of six distinct locations on three separate chips revealed 702 segmentation features resulting from thermoplastic instability during the cutting process [15]. Analysis for these measured features provided an estimate of the segmentation spacing.

Figure 16 shows histograms of chip segmentation spacing for machining on Al 6061-T6 and 1045 steel for two cases, as well as images of representative chips. The fairly normal, but somewhat broad, probability distribution of Figure 16(a) is typical of all aluminum trials examined. However, the steel trials had a long-tailed distribution, including one trial that exhibited a fairly bimodal distribution, as seen in Figure 16(b). Therefore, the average segmentation spacing was applied to calculate a rough approximation of the chip segmentation frequency.

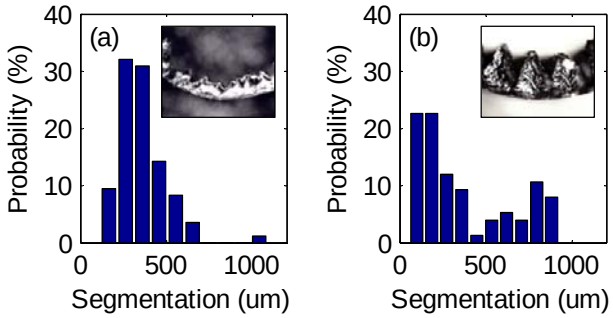

FIGURE 16 – HISTOGRAMS OF CHIP SEGMENTATION SPACING FOR (A) TRIAL 2 AND (B) TRIAL 6 OF TABLE 1

Equation (8) represents the chip segmentation frequency (f_{seg}) as a function of the part surface speed v, and the measured segmentation spacing d_{seg} multiplied by the approximate average chip compression ratio of 3.

$$f_{\text{seg}} = \frac{v}{3d_{\text{seg}}} \tag{8}$$

The compression ratio is highly dependent on several factors not discussed here, but in the following it is assumed that it remains at a constant value of 3. The resulting estimates of segmentation frequencies ranged from 1,500 Hz to 5,000 Hz, which fall within the frequency ranges of the sensors. The sensors' spectral data contain peaks that provide evidence of the segmentation frequencies.

Measuring the chip mass and calculating the chip mass flow during cutting enabled estimation of the chip breakage frequencies, that is, how frequently the cut chips break off of the workpiece during material removal. Equation (9) represents the chip breakage frequency (f_{break}) as a function of the material density ρ, the cross-sectional area of the uncut chip A, and the chip mass m.

$$f_{\text{break}} = \frac{\rho v A}{m} \tag{9}$$

For these eight trials the measured chip breakage frequencies ranged from 100 Hz to 1100 Hz.

TIME RECORD RECONSTRUCTION

With the segmentation and breakage frequencies known, custom software using band-pass filtering retained only the frequency ranges corresponding to chip breakage and segmentation. An inverse FFT then reconstructed "clean" time

records, which showed time-signature evidence of the chip segmentation and breakage. Figure 17 shows one such example where the top raw AE data plot and the bottom filtered and reconstructed AE data plot differ in amplitude scale by roughly 20x.

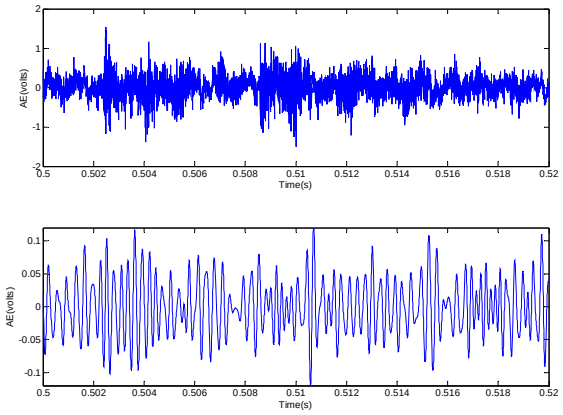

FIGURE 17 – RAW (TOP) AND RECONSTRUCTED FILTERED TIME RECORDS OF AE DATA FOR ONE TRIAL

CONCLUSIONS

The experimental data from a suite of sensors, as described here, demonstrates the potential of this method for process monitoring of machining operations. The capability of multiple sensors detecting the same phenomena also offers promise for reducing the number of sensors in the suite and perhaps focusing on the sensors that are least expensive.

ACKNOWLEDGMENTS

The authors thank Michael D. Kennedy for his assistance with the chip analysis.

REFERENCES

[1] R. Teti, *et al.*, "Advanced Monitoring of Machining Operations," *CIRP Annals - Manufacturing Technology,* vol. 59/2, pp. 717-739, 2010.

[2] S. Binsaeid, *et al.*, "Machine Ensemble Approach for Simultaneous Detection of Transient and Gradual Abnormalities in End Milling Using Sensor Fusion," *Journal of Materials Processing Technology,* vol. 209, pp. 4728-4738, 2009.

[3] A. Al-Habaibeh, *et al.*, "The Application of Force and Acoustic Emission Sensors for Detecting Tool Damage in Turning Processes," *Key Engineering Materials,* vol. 419-420, pp. 381-384, 2010.

[4] I. Kandilli, *et al.*, "Online monitoring of tool wear in drilling and milling by multi-sensor neural network fusion," *Proceedings of the 2007 IEEE International Conference on Mechatronics and Automation,* pp. 1388-94, 2007.

[5] W. D. Callister, Jr., *Materials Science and Engineering: An Introduction*, Fourth ed.: John Wiley & Sons, Inc., 1997.

[6] R. S. Figliola and D. E. Beasley, *Theory and Design for Mechanical Measurements*, Third ed.: John Wiley & Sons, Inc., 2001.

[7] D. E. Lee, *et al.*, "Precision Manufacturing Process Monitoring with Acoustic Emission," *International Journal of Machine Tools & Manufacture,* vol. 46, pp. 176-188, 2006.

[8] T. W. Hwang, *et al.*, "Acoustic Emission Monitoring of High Speed Grinding of Silicon Nitride," *Ultrasonics,* vol. 38, pp. 614-619, 2000.

[9] J. Barry and G. Byrne, "Chip Formation, Acoustic Emission and Surface White Layers in Hard Machining," *CIRP Annals - Manufacturing Technology,* vol. 51, pp. 65-70, 2002.

[10] MISTRAS Group Inc. (2010). *Complete Line of Standard Acoustic Emission Sensors*. Available: http://www.mistrasgroup.com/products/company/publications/2$Acoustic_Emission/AE_Sensor_Catalog.pdf

[11] M. A. Davies, *et al.*, "Ultrasonic Detection of Unstable Plastic Flow in Metal Cutting," *Nondestructive Characterization of Material VIII,* pp. 205 - 209, 1998.

[12] S. Rajala and J. Lekkala, "Film-type Sensor Materials PVDF and EMFi in Measurement of Cardiorespiratory Signals - A Review," *Sensors Journal, IEEE,* 2010.

[13] K. G. McConnell and P. S. Varoto, "Vibration Testing: Theory and Practice," Second ed: John Wiley & Sons, Inc, 2008, pp. 317-319.

[14] W. H. Press, *et al.*, *Numerical Recipes in FORTRAN: The Art of Scientific Computing*, Second ed.: Cambridge University Press, 1992.

[15] R. Ivester, *et al.*, "Measuring Chip Segmentation by High-Speed Microvideography and Comparison to Finte-Element Modeling Simulations," *Proceedings: 10th CIRP International Workshop on Modeling of Machining Operations,* 2007.

